Journal of Welding Technology
P-ISSN: 2716-1471 | E-ISSN: 2716-0475
http://e-jurnal.pnl.ac.id/Welding_Technology

Numerical Framework for Multi-Pass SMAW Pre-WPS Development on SA-36 Low Carbon Steel

Regan Rahadian Pambudi*, Ayende
Department of Refinery Mechanical Engineering, PEM Akamigas,
Cepu 58315, Central Java, Indonesia
Corresponding author: reganrahasia@gmail.com

Article Processing Dates:
Received 2026-05-31
Accepted 2026-06-16
Available online 2026-06-20

Keywords:
SMAW, multi-pass welding, Rosenthal 2D, finite element analysis, pre-WPS, ASME BPVC Section IX

Abstract

Multi-pass SMAW on low carbon steel demands precise parameter control to ensure joint integrity and qualification compliance. Trial-and-error WPS development is material-intensive and time-consuming, particularly where heat input management across passes is critical. This study proposes a numerical framework combining Carbon Equivalent (CET) analysis, Rosenthal 2D thermal modeling via MATLAB with SmartWeld suite, and thermo-mechanical FEA to determine preliminary welding parameters prior to experimental qualification. Parameters are validated on SA-36 plate using a 4-pass SMAW procedure qualified under ASME BPVC Section IX, with NDT per ASME BPVC Section V. Tensile strengths of 530.90 MPa and 503.99 MPa exceed the 400 MPa minimum, all bend specimens pass without rejectable discontinuities, and FEA deformation prediction of 1.59 mm against a measured 2.01 mm demonstrates conservative predictive capability suitable for preliminary parameter screening. Unlike conventional trial-and-error qualification, this framework integrates three analytical methods into a structured pre-screening workflow, reducing material consumption and qualification iterations prior to experimental testing.

1. Introduction

Shielded Metal Arc Welding (SMAW) remains widely adopted in industrial pipeline and pressure vessel construction due to its operational flexibility, equipment portability, and cost efficiency [1], [2], [3], [4]. In multi-pass welding configurations, each successive pass introduces a distinct heat input that cumulatively influences metallurgical characteristics, joint geometry, and residual stress distribution. Poor parameter selection leads to defects including incomplete penetration, porosity, and excessive distortion, all of which compromise structural integrity (Fig. 1). [2], [4], [5], [6], [7], [8]

Fig. 1. Effect Of Poor Welding Parameter Selection [8]

Welding Procedure Specification (WPS) development conventionally relies on iterative experimental qualification, a process that is both material-intensive and time-consuming. Several studies have explored analytical and numerical approaches to reduce this dependency. Rosenthal's moving heat source model provides a closed-form solution for thermal distribution in welding, while Finite Element Analysis (FEA) has demonstrated capability in predicting thermo-mechanical responses including deformation and stress fields in multi-pass configurations [8], [9], [10]. However, systematic integration of weldability screening, thermal prediction, and deformation simulation as a unified pre-WPS framework remains relatively limited in the literature reviewed.

While Trupiano et al. [10] and Zhang and Yang [8] addressed residual stress simulation and numerical parameter optimization respectively, neither framed their approach as a qualification-oriented pre-WPS workflow. This study addresses that gap by integrating CET weldability analysis, Rosenthal 2D thermal modeling, and thermo-mechanical FEA using CalculiX into a unified pre-WPS screening framework for multi-pass SMAW on SA-36 low carbon steel, validated experimentally under ASME BPVC Section IX requirements [14].

2. Research Methods

2.1. Material and Weldability Assessment

The base material used is an 8 mm thick SA-36 low carbon steel plate. SA-36 classification is shown as in Fig. 2

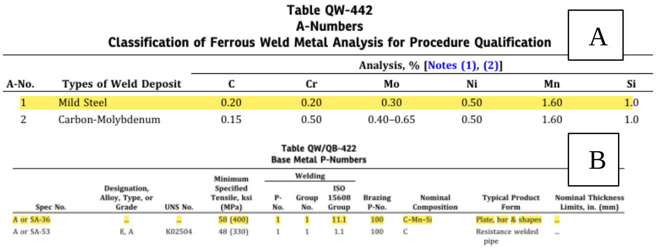

Table QW-442
A-Numbers
Classification of Ferrous Weld Metal Analysis for Procedure Qualification

A

A-No.	Types of Weld Deposit	Analysis, % [Notes (1), (2)] C	Cr	Mo	Ni	Mn	Si
1	Mild Steel	0.20	0.20	0.30	0.50	1.60	1.0
2	Carbon-Molybdenum	0.15	0.50	0.40–0.65	0.50	1.60	1.0

Table QW/QB-422
Base Metal P-Numbers

B

Spec No.	Designation, Alloy, Type, or Grade	UNS No.	Minimum Specified Tensile, ksi (MPa)	Welding P-No.	Welding Group No.	Welding ISO 15608 Group	Brazing P-No.	Nominal Composition	Typical Product Form	Nominal Thickness Limits, in. (mm)
A or SA-36	...	...	58 (400)	1	1	11.1	100	C–Mn–Si	Plate, bar & shapes	...
A or SA-53	E, A	K02504	48 (330)	1	1	1.1	100	C	Resistance welded pipe	...

Fig. 2. SA-36; (a) Max Chemical Compositions, (b) Tensile

Weldability is assessed through Carbon Equivalent (CET) calculation to evaluate susceptibility to hydrogen-induced cracking and heat affected zone (HAZ) hardening using equation (1). [11], [12], [13]

$$CE = C + \frac{Mn + Mo}{10} + \frac{Cr + Cu}{20} + \frac{Ni}{40} \qquad (1)$$

Where C, Mn, Mo, Cr, Cu, and Ni are elemental compositions in wt%.

To determine the preheating requirement, CET threshold corresponding to an 8 mm plate thickness was assessed based on the limit values shown in Table 1. [13]

Table 1. Maximum Plate Thickness For CET%.

CET (%)	Max Plate Thickness (mm)
0.18	60
0.22	50
0.26	40
0.31	30
0.34	20
0.38	12
0.40	8

2.2. Thermal Analysis and Heat Input Determination

The required number of passes is estimated from plate thickness and electrode diameter using equation (2). [14]

$$np = \frac{tm}{de} + 1 \tag{2}$$

Where *np* is the required number of passes, *tm* is plate thickness (mm), and *de* is the smallest electrode diameter used (mm).

Thermal distribution for each pass is modeled using the Rosenthal 2D moving heat source equation (3). [8]

$$\frac{2\pi(T - T_0)kg}{Q} = \exp\left(\frac{Vx}{2\alpha}\right) K_0 \left(\frac{Vr}{2\alpha}\right) \tag{3}$$

Rosenthal analysis is implemented using MATLAB with SmartWeld suite to generate isothermal profiles, HAZ thermal cycles, and penetration depth predictions per pass. An interpass temperature of 120°C is applied across passes 2 through 4. [15]

Combinations of welding current, voltage, and travel speed were iteratively adjusted until the target penetration depth was achieved while maintaining the heat input within the specified limits. The heat input for each pass was calculated using Equation (4). [16]

$$Q = \frac{V \times A \times 60}{u} \tag{4}$$

Where Q is heat input per unit weld length (kJ/mm), V is arc voltage (Volt), A is welding current (Ampere), and u is travel speed (mm/min).

Each pass must maintain heat input between 0.5 kJ/mm and 4.0 kJ/mm to avoid weld defects and HAZ metallurgical degradation respectively. [14]

To validate the Rosenthal 2D thermal predictions, a non-contact thermal gun measured surface temperatures at the melt isotherm (T melt), T1, and T2 boundary positions along the plate width, extracted from the isothermal profiles in Fig. 6 through Fig. 9, enabling direct comparison between predicted and measured thermal boundaries per pass.

2.3. Thermo-Mechanical Finite Element Analysis

FEA simulation is performed using CalculiX solver. The weld joint is modeled in 3D based on actual specimen dimensions, meshed using Netgen at 0.3 mm element size, yielding 82,971 nodes. Fig. 3 illustrates the three-dimensional (3D) geometry and finite element mesh of the Cu–SS316L butt-welded joint used in the thermal simulation. The moving heat source was subsequently applied along the weld centerline, as illustrated in Fig. 4.

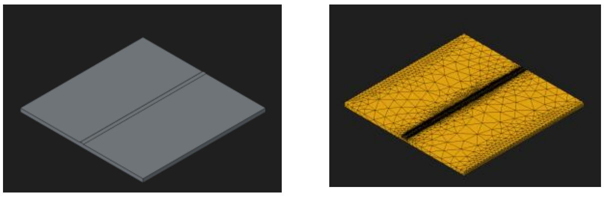
(a) (b)

Fig. 3. Weld Joint; (a) 3D Model, (b) Mesh Model

Mild steel properties are assigned as representative of SA-36. Heat input was applied as a moving surface heat flux along the weld path from the total heat input associated with each welding pass.

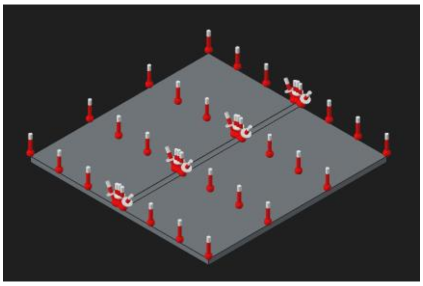
Fig. 4. Weld Joint Thermal Load

Total heat input across all passes is calculated using equation (5).

$$Qt = \sum_{i=1}^{n} Qi \tag{5}$$

Where Qt is total accumulated heat input across all passes (kJ/mm), Qi is heat input at pass i (kJ/mm), n is the total number of passes, and i is the pass number.

Using FEA, the deformation and von Mises stress distributions are extracted from the simulation output to evaluate the thermo-mechanical response of the weld joint during welding. [8]

To validate the FEA, post welding deformation was measured at the weld centerline and compared against the FEA prediction using a calibrated angle gauge.

2.4. Experimental Qualification

Welding is performed on SA-36 plate specimens using SMAW with the numerically derived pre-WPS parameters. Joint design follows a groove weld configuration with a calculated pass sequence in Fig. 5.

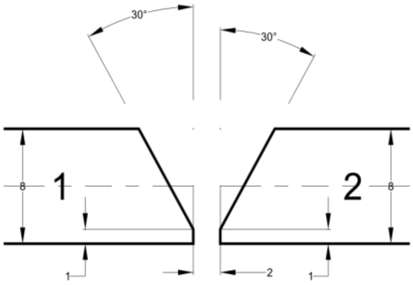

Fig. 5. Weld Joint Design (mm)

During welding, current and voltage are monitored using a clamp meter, travel speed is tracked via stopwatch, and interpass temperature is verified using a thermal imager.

Following welding, NDT was performed in accordance with ASME BPVC Section V, including visual inspection (VT), liquid penetrant testing (PT), and ultrasonic testing (UT). All inspection and destructive testing equipment were calibrated prior to testing. Acceptance criteria followed ASME BPVC Section IX QW-195.2.2 for PT and QW-191.2.2 for UT. Destructive testing was then conducted per ASME BPVC Section IX using two tensile and four bend specimens (two face-bend and two root-bend) prepared in accordance with QW-463.1(a). Acceptance criteria followed QW-153.1 for tensile tests and QW-163 for bend tests. [16], [17]

3. Result and Discussion

3.1. Material and Weldability Assessment

Based on the measured chemical composition of SA-36, the Carbon Equivalent (CET) is calculated to evaluate preheat requirements and susceptibility to hydrogen-induced cracking.

$$CET = C + \frac{Mn + Mo}{10} + \frac{Cr + Cu}{20} + \frac{Ni}{40}$$

$$CET = 0.16 + \frac{1.28 + 0.24}{10} + \frac{0.16 + 0.08}{20} + \frac{0.4}{40}$$

$$CET = 0{,}334 < 0{,}4 \; for\; 8\; mm\; plate$$

CET falls below the 0.40 threshold for 8 mm plate, confirming no preheat is required under nominal conditions.

3.2. Pre-WPS Parameter Determination

Using the number of passes formula, the required pass count is determined from the 8 mm plate thickness and the smallest available electrode diameter of 2.6 mm. Electrodes E7016 LB-52U with diameters of 2.6 mm and 3.2 mm are selected, and welding parameters for each pass are kept within the manufacturer's operational boundaries.

$$np = \frac{tm}{de} + 1$$

$$np = \frac{8\; mm}{2.6\; mm} + 1$$

$$np = 4\; pass$$

Plate thickness of 8 mm with a 2.6 mm electrode diameter yields a required pass count of 4.

Heat input per pass is iteratively adjusted using MATLAB with SmartWeld suite until the target penetration depth is achieved per pass. Penetration depth and isothermal profiles are shown in Fig. 6-9.

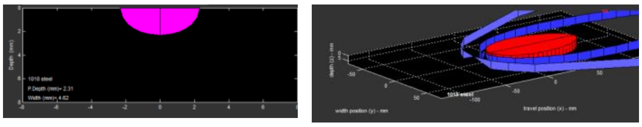

(a) (b)

Fig. 6. 1st Pass; (a) *Depth*, (b) *Path*
(T melt; 1530 °C, 1; 920 °C, 2; 320 °C)

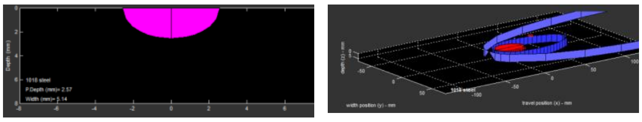

(a) (b)

Fig. 7. 2nd Pass; (a) *Depth*, (b) *Path*
(T melt; 1530 °C, 1; 960 °C, 2; 400 °C)

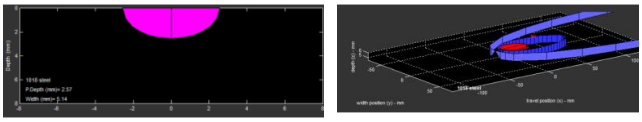

(a) (b)

Fig. 8. 3rd Pass; (a) *Depth*, (b) *Path*
(T melt; 1530 °C, 1; 960 °C, 2; 400 °C)

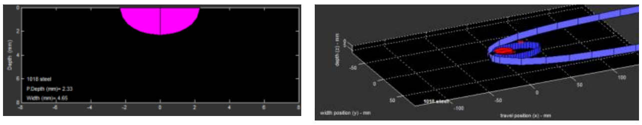

(a) (b)

Fig. 9. 4th Pass; (a) *Depth*, (b) *Path*
(T melt; 1530 °C, 1; 960 °C, 2; 400 °C)

SmartWeld Rosenthal analysis produces the parameter set in Table 2, with heat input ranging from 2.59 to 3.94 kJ/mm across all passes, all within the 0.5 to 4.0 kJ/mm allowable range and the manufacturer's operational boundaries for E7016 LB-52U.

Table 2. SmartWeld Welding Parameter.

Parameter	1st	2nd	3rd	4th
Heat Input (kJ/mm)	3.94	2.88	2.88	2.59
Ampere (A)	60	80	85	90
Voltage (V)	23	24	24	24
Travel Speed (mm/s)	0.35	0.6	0.7	0.8
Heat Input > 4 kJ/mm	No	No	No	No
Heat Input < 0.5 kJ/mm	No	No	No	No
Outside Manufacturer's Operational (60-90A)	No	No	No	No

3.3. FEA Deformation and Stress Prediction

Total heat input across all passes is summed using the cumulative heat input equation.

$$Qt = \sum_{i=1}^{n} Qi$$

$$Qt = 3.94 + 2.88 + 2.88 + 2.59 \frac{kJ}{mm}$$

$$Qt = 12.29 \frac{kJ}{mm}$$

Thermo-mechanical FEA is then performed with CalculiX to predict deformation and von Mises stress distribution resulting from the multi-pass thermal cycle (Fig 10-11).

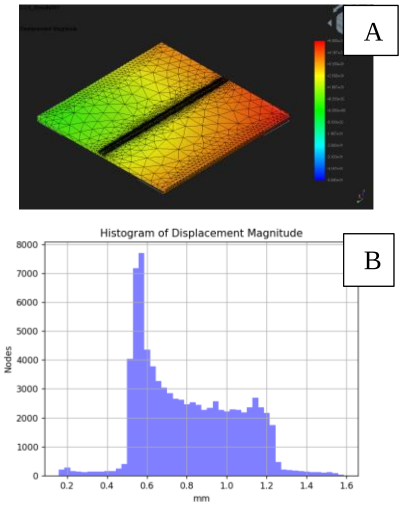

Fig. 10. Deformation; (a) Heatmap, (b) Histogram

Displacement analysis shows maximum deformation of 1.59 mm at the weld centerline, with distribution ranging from 0.6 mm to 1.2 mm across the plate.

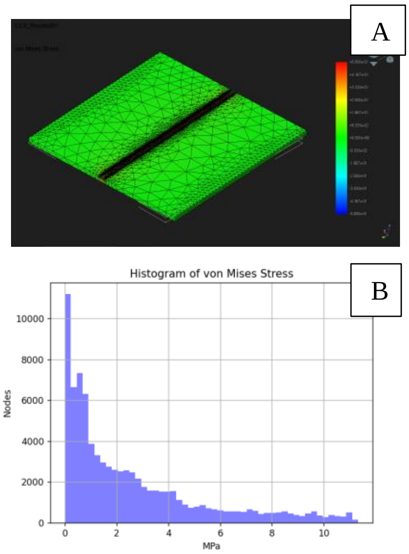

Fig. 11. Stress; (a) Heatmap, (b) Histogram

Maximum von Mises stress remains relatively low and is concentrated near the weld region, indicating that the selected thermal cycle is unlikely to induce significant localized yielding. The stress distribution remains concentrated near the weld region and supports the suitability of the selected pre-WPS parameters for experimental qualification.

3.4. Experimental And Qualification Results

Using the pre-WPS parameters derived from Rosenthal 2D thermal analysis and FEA simulation, the weld coupon is fabricated on SA-36 plate using SMAW with a 4-pass groove weld sequence.

Current and voltage are monitored using a clamp meter, travel speed tracked via stopwatch, and interpass temperature verified using a thermal imager to ensure parameters remain within pre-WPS bounds throughout execution. The joint pass and welding results are shown in Fig. 12

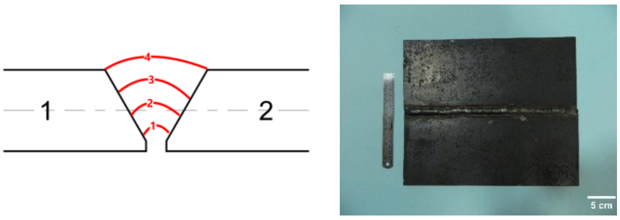

(a) (b)

Fig. 12. Welding; (a) Joint Pass, (b) Result

The Comparison between predicted and measured thermal boundary profiles per pass is shown in Fig. 13 through Fig. 16.

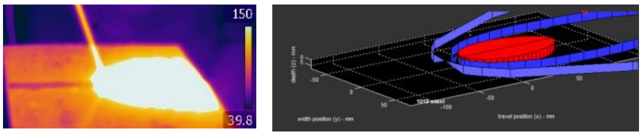

(a) (b)

Fig. 13. 1st Pass; (a) *Depth*, (b) *Path*

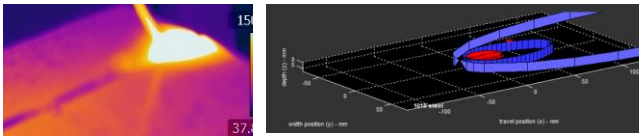

(a) (b)

Fig. 14. 2nd Pass; (a) *Depth*, (b) *Path*

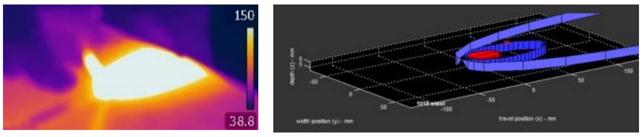

(a) (b)

Fig. 15. 3rd Pass; (a) *Depth*, (b) *Path*

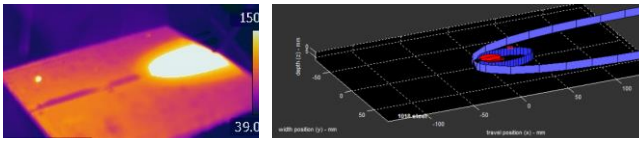

(a) (b)

Fig. 16. 4tb Pass; (a) *Depth*, (b) *Path*

FEA predicts maximum deformation of 1.59 mm against a measured value of 2.01 mm post-welding, yielding a deviation of 20.9% as shown in Fig. 17

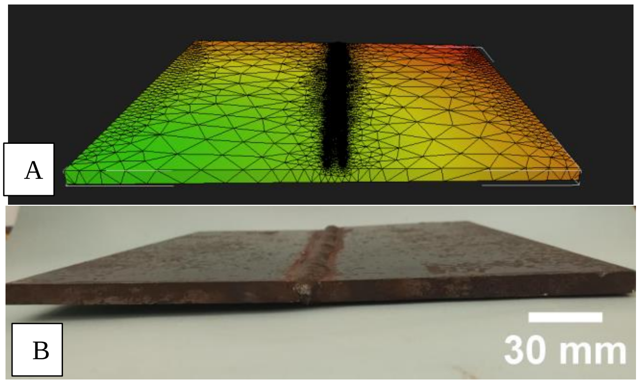

Fig. 17. Deformation; (a) FEA, (b) Post-Welding

The deviation is attributed to simplified boundary conditions in the FEA model and real-time parameter adjustments by the welder, though the prediction remains conservative and directionally accurate, confirming its utility as a preliminary screening tool. Penetrant test indication in Fig. 18.

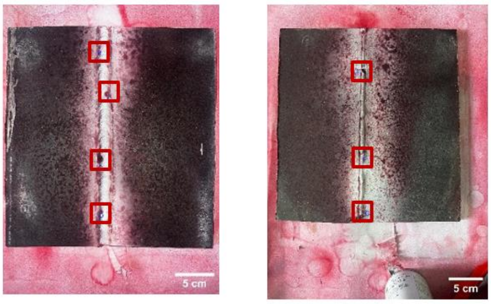

(a) (b)

Fig. 18. Penetrant Test Indication 1-7; (a) Face, (b) Root

Liquid penetrant testing identified seven surface indications associated with porosity and incomplete penetration on the face and root surfaces. All fall within the 5 mm maximum limit per ASME BPVC Section IX QW-195.2, with no linear indications detected. Ultrasonic test indication in Fig. 19

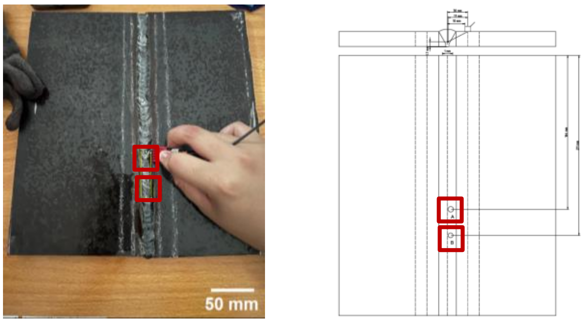

(a) (b)

Fig. 19. Ultrasonic Test Indication 1 and 2;
(a) Reading, (b) Indication Point

Ultrasonic testing identified two slag inclusion indications at points A (1.9 mm) and B (2.7 mm), both below the 3 mm acceptance limit specified by ASME BPVC Section IX QW-191.2. No rejectable indications are present.

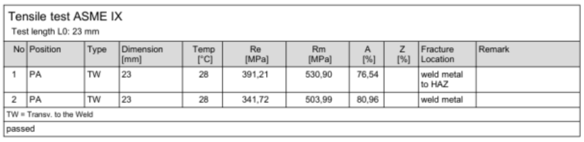

Tensile test ASME IX
Test length L0: 23 mm

No	Position	Type	Dimension [mm]	Temp [°C]	Re [MPa]	Rm [MPa]	A [%]	Z [%]	Fracture Location	Remark
1	PA	TW	23	28	391,21	530,90	76,54		weld metal to HAZ	
2	PA	TW	23	28	341,72	503,99	80,96		weld metal	

TW = Transv. to the Weld

passed

Fig. 20. Tensile Test Result (Tensile No. 1 and No. 2)

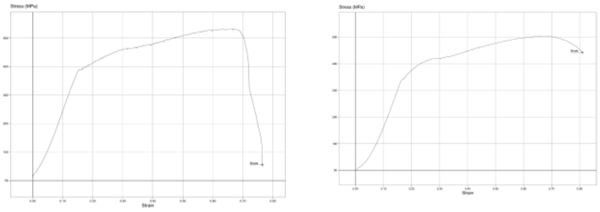

(a) (b)

Fig. 21. Tensile Test Graph; (a) No 1, (b) No 2

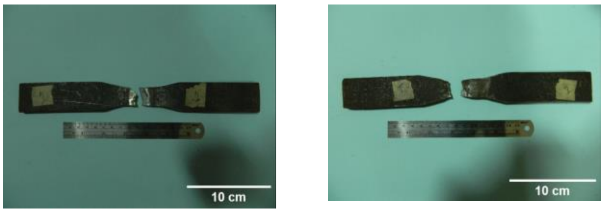

(a) (b)

Fig. 22. Tensile Test Result; (a) No 1, (b) No 2

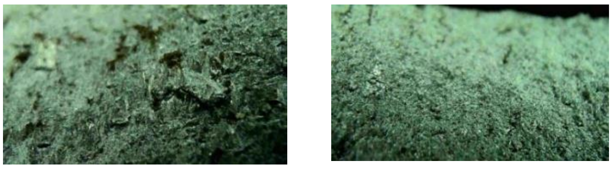

(a) (b)

Fig. 23. Tensile Test Macro Surface; (a) No 1, (b) No 2

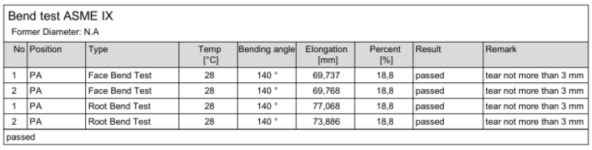

Bend test ASME IX
Former Diameter: N.A

No	Position	Type	Temp [°C]	Bending angle	Elongation [mm]	Percent [%]	Result	Remark
1	PA	Face Bend Test	28	140 °	69,737	18,8	passed	tear not more than 3 mm
2	PA	Face Bend Test	28	140 °	69,768	18,8	passed	tear not more than 3 mm
1	PA	Root Bend Test	28	140 °	77,068	18,8	passed	tear not more than 3 mm
2	PA	Root Bend Test	28	140 °	73,886	18,8	passed	tear not more than 3 mm

passed

Fig. 24. Bending Test Result (FBa, FBb, RBc, RBd)

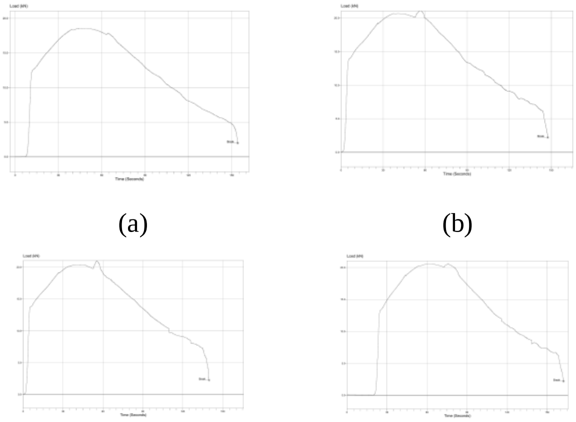

(a) (b)

(c) (d)

Fig. 25. Bending Test Graph;
(a) FB1, (b) FB2, (c) RB1, (d) RB2

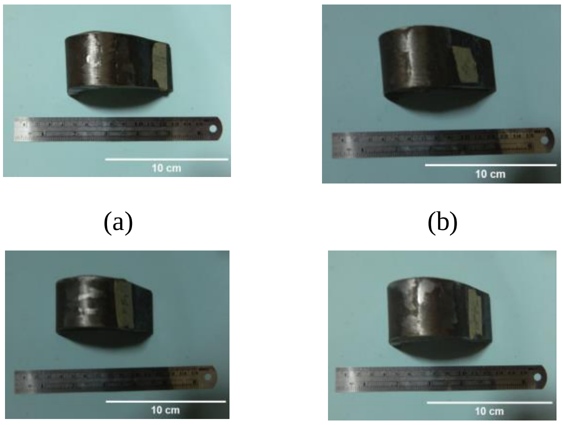

(a) (b)

(c) (d)

Fig. 26. Bending Test Result;
(a) FB1, (b) FB2, (c) RB1, (d) RB2

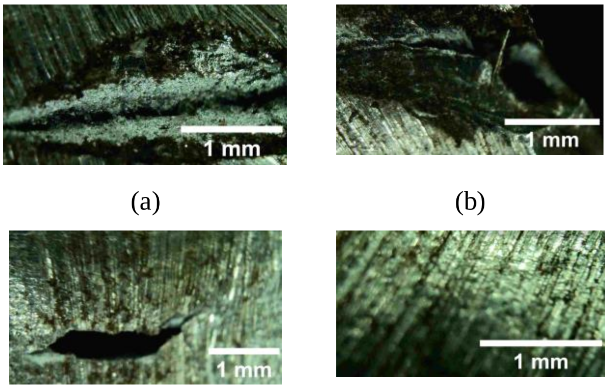

(a) (b)

(c) (d)

Fig. 27. Bending Test Macro Surface;
(a) FB1, (b) FB2, (c) RB1, (d) RB2

Tensile testing yields strengths of 530.90 MPa and 503.99 MPa with elongations of 76.54% and 80.96% respectively, both exceeding the SA-36 minimum of 400 MPa. Fracture occurs at the weld metal to HAZ interface, and both specimens meet acceptance criteria of ASME BPVC Section IX QW-153.1. Bend testing on four specimens, two face bend and two root bend, shows no open discontinuities exceeding 3 mm in the weld or HAZ region after 180° deflection, all specimens meet the acceptance criteria of ASME BPVC Section IX QW-163. Both results satisfy ASME BPVC Section IX acceptance criteria, confirming the procedure is qualified for WPS issuance.

4. Conclusions.

An integrated numerical framework consisting of CET weldability assessment, Rosenthal 2D thermal modeling, and thermo-mechanical FEA was developed for pre-WPS parameter determination of multi-pass SMAW on SA-36 steel. The framework successfully identified a feasible 4-pass welding procedure, provided conservative deformation predictions, and produced welding parameters that satisfied all ASME BPVC Section IX qualification requirements. The results demonstrate that numerical analysis can serve as an effective preliminary screening tool, reducing reliance on trial-and-error during WPS development while supporting successful experimental qualification.

References.

[1] M. Dioktyanto, H. Abdullah, Y. P. Dewi, I. N. Rokhim, and T. J. Kuswanto, "Current progress on wire-arc and welding-based additive manufacturing with its potential application: a review".

[2] P. K. Baghel, "Effect of SMAW process parameters on similar and dissimilar metal welds: An overview," *Heliyon*, vol. 8, no. 12, p. e12161, Dec. 2022, doi: 10.1016/j.heliyon.2022.e12161.

[3] A. Ayende, Moch. B. Bahtiar, H. Kotrisna, S. Damayanti, R. D. Santoso, and M. Bagas A. P., "Experimental Study of Oil and Gas Pressure Vessel Welding Using The Shielded Metal Arc Welding Process," *Sci. Contrib. Oil Gas*, vol. 48, no. 2, pp. 41–51, Aug. 2025, doi: 10.29017/scog.v48i2.1775.

[4] M. H. Sar, O. S. Barrak, and S. K. Hussain, "Effect of Multi-pass SMAW Welding on the Surface Hardness and Microstructure of Carbon Steel AISI 1050," *IOP Conf. Ser. Mater. Sci. Eng.*, vol. 1105, no. 1, p. 012058, Jun. 2021, doi: 10.1088/1757-899X/1105/1/012058.

[5] Universitas Lancang Kuning, Pekanbaru, Indonesia *et al.*, "Influence of SMAW Welding Current Variations on the Tensile Strength of API 5L Grade B Pipe," *J. Ocean Mech. Aerosp. -Sci. Eng.- JOMAse*, vol. 69, no. 3, pp. 253–258, Nov. 2025, doi: 10.36842/jomase.v69i3.560.

[6] T. Lei, S. Gong, and C. Wu, "A Multi-Layer Multi-Pass Weld Bead Cross-Section Morphology Extraction Method Based on Row–Column Grayscale Segmentation," *Materials*, vol. 17, no. 19, p. 4683, Sep. 2024, doi: 10.3390/ma17194683.

[7] Y. Cai, G. Yu, J. Yu, and Y. Ji, "Orbital-Based Automatic Multi-Layer Multi-Pass Welding Equipment for Small Assembly Plates," *Appl. Sci.*, vol. 14, no. 23, p. 10878, Nov. 2024, doi: 10.3390/app142310878.

[8] K. Zhang and Z. Yang, "The effects of welding process parameters on properties of welded joint for enhancing welding structural integrity using simulation and experimental methods," *J. Mater. Res. Technol.*, vol. 38, pp. 2113–2125, 2025, doi: https://doi.org/10.1016/j.jmrt.2025.08.067.

[9] S. Afkhami *et al.*, "Experimental-numerical insights into heat-affected zone failure of welded aluminum alloys," *Weld. World*, Feb. 2026, doi: 10.1007/s40194-026-02394-2.

[10] S. Trupiano, V. G. Belardi, P. Fanelli, L. Gaetani, and F. Vivio, "A novel modeling approach for multi-passes butt-welded plates," *J. Therm. Stress.*, vol. 44, no. 7, pp. 829–849, Jul. 2021, doi: 10.1080/01495739.2021.1916415.

[11] J. N. DuPont, J. C. Lippold, and S. D. Kiser, *Welding Metallurgy and Weldability of Nickel-Base Alloys*, 1st ed. Wiley, 2009. doi: 10.1002/9780470500262.

[12] B. ÇiÇek and Y. Sun, "Weldability and Service Conditions of Steels in Thermal Power Plant Applications," 2022.

[13] W. Uwer, D H., "Anwendung des Kohlenstoffäquivalents CET zur Berechnung von Mindestvorwärmtemperaturen für das kaltrißsichere Schweißen von Baustählen." DVS, Germany, 2024.

[14] A. Trindade, "Estimating the Number of Passes in the Weld Deposition as a Function of the Heat Input," *Curr. Eng. Lett. Rev.*, vol. 02, p. e2666948X357790, Jun. 2025, doi: 10.2174/012666948X357790241217113737.

[15] H. Geng, J. Li, J. Xiong, and X. Lin, "Optimisation of interpass temperature and heat input for wire and arc additive manufacturing 5A06 aluminium alloy," *Sci. Technol. Weld. Join.*, vol. 22, no. 6, pp. 472–483, 2017, doi: 10.1080/13621718.2016.1259031.

[16] American Society of Mechanical Engineers, *ASME Boiler and Pressure Vessel Code, Section IX: Welding, Brazing, and Fusing Qualifications*. New York, NY, USA: The American Society of Mechanical Engineers, 2025.

[17] American Society of Mechanical Engineers, *ASME Boiler and Pressure Vessel Code, Section V: Nondestructive Examination*. New York, NY, USA: The American Society of Mechanical Engineers, 2025.